RSC Advances

PAPER

View Article Online
View Journal | View Issue



Cite this: *RSC Adv.*, 2015, **5**, 36185

# Synthesis of a flower-like CuS/ZnS nanocomposite decorated on reduced graphene oxide and its photocatalytic performance†

Xiao-Hui Guan,[a] Liu Yang,[a] Xin Guan[b] and Guang-Sheng Wang*[b]

A series of graphene-based materials composed of flower-like CuS/ZnS (CZS) microspheres and reduced graphene oxide (rGO) with different weight ratios have been fabricated *via* a two-step approach, in which CZS was synthesized first by a hydrothermal method, and then combined with rGO *via* a sonochemical process to form CuS/ZnS/rGO (CZS/rGO) composites. The photocatalytic activity was studied by photodegradation of methylene blue (MB) in the presence of hydrogen peroxide ($H_2O_2$). The results showed that all the graphene-based photocatalysts exhibited enhanced catalytic activity, compared to pure CuS/ZnS (CZS) composites. When the weight ratio of graphene in the composite materials was 20 wt%, the composite presented the highest photocatalytic efficiency, which could eliminate more than 99% of MB within 20 min and the photocatalytic efficiency could be kept at about 99% of the original photocatalytic efficiency after three cycles.

Received 6th March 2015
Accepted 16th April 2015

DOI: 10.1039/c5ra04030b

www.rsc.org/advances



## Introduction

Semiconductor nanomaterials have gained considerable interest in the applications in environmental remediation and energy conversion, such as photocatalytic degradation of organic and toxic pollutants in water and air, water splitting into $H_2$ and photoelectrochemical solar cells and so on.[1–3] They have shown many excellent properties, such as high photocatalytic efficiency, great economic interest, harmlessness to the environment without introducing other undesirable by-products, and the capability to utilize solar energy, which is considered to be the most important merit. In the past few decades, more and more investigations have been conducted to fabricate new-type, cost-efficient and clean semiconductor photocatalysts that response to both UV and visible lights to eliminate organic contaminants, especially non-biodegradable ones.[4] Metal sulfides have proven to be excellent photo-reactive catalysts.[5] Particularly, zinc sulfide (ZnS), one kind of nontoxic and abundant chalcogenide materials with a direct wide-gap, is a promising candidate as photocatalysts in environmental protection, which can be ascribed to its unique properties: rapid generation of electron–hole pairs by photo-excitation,[6] highly negative reduction potentials of excited elections,[7] and prominent stability against the photo-corrosion;[8] However, its relatively wide band gap (~3.72 eV or ~3.77 eV for the cubic zinc blende and hexagonal wurtzite phase respectively) is too large to utilize visible light. In addition, the fast recombination rate of electron–hole pairs dramatically restricts its applications as photocatalyst.[9] Copper sulfide (CuS) is a p-type semiconductor with narrow band gap, and simultaneously it exhibits low reflectance in the visible region and relatively high reflectance in the near-infrared region, which enables CuS to effectively utilize the visible light energy.[10,11] Hence, it is a facile strategy to load ZnS on the CuS surface to obtain a novel hybrid photocatalyst, CuS/ZnS (CZS), with enhanced UV and visible-light-driven photocatalytic activity. CZS nanocomposite not only can facilitate the separation of photoinduced electron–hole pairs, which ensures more charge carriers migrate to the surface of the photocatalyst to trigger redox reactions, but also shows extensive adsorption range and improved adsorption intensity of solar energy compared to the bare CuS and ZnS.[12] Although the integration of CuS and ZnS has already achieved enormous progress in improving the photocatalytic performance, more efforts and attention should be devoted to enhancing the poor adsorption capacity and further promoting the separation rate of photo-generated electron–hole pairs, which substantially inhibit the practical applications of the photocatalyst.

Graphene, a two dimensional carbon material, consists of a flat monolayer of $sp^2$-hybridized carbon atoms that are tightly packed into a honeycomb lattice.[13] To investigate and apply graphene and graphene-based nanomaterials more comprehensively, plenty of feasible approaches have been proposed including physical and chemical methods to synthesize graphene with remarkable properties, such as mechanical exfoliation,[14] chemical vapour deposition route,[15] epitaxial growth,[16] electrochemical exfoliation of graphite[17] and reduction of

[a]*School of Chemical Engineering, Northeast Dianli University, Jilin 132000, PR China*
[b]*Key Laboratory of Bio-Inspired Smart Interfacial Science and Technology of Ministry of Education, School of Chemistry and Environment, Beihang University, Beijing 100191, PR China. E-mail: wanggsh@buaa.edu.cn*

† Electronic supplementary information (ESI) available. See DOI: 10.1039/c5ra04030b

exfoliated graphene oxide (GO)[18,19] and so on. Among these synthetic routes, reduction of the exfoliated GO sheets is thought to be of more importance and practical application value, owing to its economical efficiency and high yield for the mass production of graphene. What's more important, reduced graphene oxide (rGO) possesses more reactive oxygen-containing functional groups in comparison to the products synthesized by other routes, which is favorable to fabricating functionalized graphene-based nanomaterials.[20,21] In recent years, graphene-based semiconductor nanomaterials used in photocatalytic field have aroused tremendous attention due to its outstanding properties: fast electron conductivity, large specific surface area, high optical transparency, good mechanical strength and high thermal conductivity. The roles of graphene playing in the hybrid photocatalysts can be summarized as follows. Firstly, the two-dimensional platform structure of graphene makes it a suitable substrate for the uniform decoration and immobilization of semiconductor particles.[22,23] Evidently, the homogeneous dispersion of nanoparticles on the graphene sheets can hinder their aggregation effectively. Meanwhile, it is also able to inhibit the graphene sheets from aggregating, which can ensure the large specific surface area of the hybrid photocatalysts. Secondly, graphene, existing in the hybrid photocatalysts, is beneficial to transferring the photogenerated electrons from the semiconductor to the surface of the photocatalysts to participate in redox reactions, and suppressing the recombination of the electrons and holes due to its superior electrical conductivity.[24,25] Finally, graphene possesses great adsorption capacity for organic molecules because of its large surface area and the strong $\pi$–$\pi$ interaction between graphene and organic molecules.[26,27] Therefore, assembling CZS particles on the graphene sheets to synthesize a novel graphene-based photocatalyst, CZS/rGO, is of great significance for the improvement of photocatalytic performance and application in environmental remediation.

Herein, we present the fabrication of CZS/rGO composites with different weight ratios of rGO *via* an ultrasound assisted chemical method. CZS with novel hierarchical nanostructure was synthesized *via* a hydrothermal process, reported by our group.[28] And GO was obtained through a modified Hummer's method.[29] Subsequently, the as-prepared photocatalysts were used to photodegrade methylene blue (MB) in the presence of hydrogen peroxide ($H_2O_2$). Furthermore, all the composites we prepared were characterized carefully, and the possible mechanism of photocatalytic reaction was put forward in this paper as well. According to the final results, all the graphene-based photocatalysts are of better photocatalytic performance than pure CZS composite.

# Experimental

Graphite powder was purchased from Alfa Aesar. The other chemicals were of analytical grade and purchased from Tianjin Guangfu Fine Chemical Research Institute. All the reagents were used as received without any further purification. The water we used in the research was double distilled water.

### Preparation of CZS/rGO composites

GO was prepared by a modified Hummer's method and then reduced through a chemical reduction route using hydrazine as the reducing agent.[29] And one-pot hydrothermal approach was utilized to synthesize CZS. In our previous studies, CZS with $Zn^{2+}/Cu^{2+}$ molar feed ratio of 0.4 exhibited the most preeminent photocatalytic reactivity, so we decide to synthesize CZS with $Zn^{2+}/Cu^{2+}$ molar ratio of 0.4 and combine it with rGO consequently in this research.[28]

CZS/rGO composites were fabricated *via* a sonochemical approach. First of all, desired weight of GO and CZS were dispersed in 60 ml double distilled water under ultrasonication for 30 min at room temperature. Then hydrazine was added into the solution and stirred gently for 5 min. Afterwards, the obtained solution was heated in the oil bath with continually magnetic stirring for 2 h at 90 °C, leading to the reduction of GO to rGO. At last, the solution containing CZS and rGO was ultrasonicated again for 2 h to obtain the final product. Then the sample was centrifuged, washed with ethanol and double distilled water, and finally dried in a vacuum oven at 50 °C for 12 h. A series of CZS/rGO composites with different weight ratios of rGO (5%, 10%, 15%, 20% and 30%) were synthesized under the same condition, which were labeled as CZS/rGO-1, CZS/rGO-2, CZS/rGO-3, CZS/rGO-4 and CZS/rGO-5, respectively. The schematic illustrations for the process to synthesize CZS/rGO composites are shown in Scheme 1.

### Characterization

X-ray diffraction (XRD) characterization was conducted on a X-ray powder diffractometer (Philips X'pert Pro Super) with Cu KR radiation ($\lambda = 0.154056$ nm). The micro-morphology of the photocatalysts was obtained by scanning electron microscopy (SEM) at 20.0 keV on a JSM6510A microscope. Fourier-transform infrared (FTIR) spectra were recorded from 4000 $cm^{-1}$ to 500 $cm^{-1}$ on an FTIR spectrometer-733 (iN10MX). Raman spectra were performed on a LabRAM HR800 Laser Raman spectroscopy with 632.5 nm wavelength incident laser light. Thermal gravimetric analyses (TGA) were carried out in air on a Pyris Diamond TG analyzer (PerklinElemer Inc., U.S.A). The heating temperature range was from 50 °C to 800 °C with a heating rate of 5 °C $min^{-1}$. UV-vis adsorption spectra were used to investigate the optical properties of the photocatalysts, recorded on a UV-2550 spectrophotometer.

### Photocatalytic experiments

The photodegradation of MB was carried out to evaluate the photocatalytic performance of the as-prepared photocatalysts,

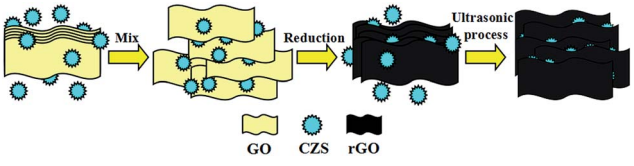


Scheme 1 Schematic description for the formation procedure of CZS/rGO.

using a homemade reactor and a 300 W Xe lamp as the light source. First of all, 0.1 g sample was added into 100 ml MB solution of 30 mg $L^{-1}$ under stirring. Subsequently, the solution was sonicated for 5 min and continuously stirred for 15 min in the dark, which would be of benefit to the complete dispersion of photocatalyst powder in the solution. Then, under magnetic stirring, 2 ml $H_2O_2$ was injected into the above solution, and meanwhile the reaction was triggered by the irradiation (250 nm < $\lambda$ < 780 nm) of the Xe lamp placed 66 cm away from the reactor. Finally, 1 ml of solution was taken out at specific time intervals, diluted to 6 ml with double distilled water, and centrifuged to remove the residual sample. The concentration of MB was analyzed by a UV-vis absorption spectrometer at 663 nm. In order to compare the photocatalytic activity of the photocatalysts we synthesized with CZS, the experimental condition was similar as reported by our group previously.[28]

## Results and discussion

As shown in Fig. 1, the molecular structure of GO and the reduction of GO to rGO were affirmed by FTIR spectra. According to the Fig. 1(a), several characteristic bands of GO associated with oxygen-containing functional groups can be recognized apparently. The band at 3400 $cm^{-1}$ belongs to the O–H stretching vibration. The C=O vibration of carboxyl is observed at 1726 $cm^{-1}$. The H–O–H bending vibration of absorbed $H_2O$ molecules and skeletal ring vibration of graphitic domains can be seen at 1620 $cm^{-1}$. Additionally, the peak at 1221 $cm^{-1}$ and 1050 $cm^{-1}$ can be attributed to the epoxy C–O stretching vibration and alkoxy C–O stretching vibration, respectively.[30,31] Nevertheless, the FTIR spectrum of CZS/rGO-4 exhibits no characteristic peaks of GO as shown in Fig. 1(a) except the weak C–O vibration at 1221 $cm^{-1}$, indicating that the oxygen-containing functional groups on GO had been successfully reduced by hydrazine. In addition, CZS/rGO-4 shows similar peaks to the result in the spectrum of CZS in cruve c, demonstrating that the graphene-based composite contained CZS.

Raman spectroscopy has already been widely applied to investigate carbon materials. The Raman spectra of GO and CZS/rGO-4 are shown in Fig. 2. Both of the spectra have two strong peaks, D and G bands, which correspond to the vibration of carbon atoms in disorder or defect sites and in-phase vibration of $sp^2$-bonded carbon atoms respectively.[32] For the spectrum of GO (curve a in Fig. 2), the D and G bands appear at 1331 $cm^{-1}$ and 1581 $cm^{-1}$, while for rGO in CZS/rGO-4 (curve b in Fig. 2), the two bands shift to 1335 $cm^{-1}$ and 1583 $cm^{-1}$. Apparently, the intensity ratio of D and G bands ($I_D/I_G$) for CZS/rGO-4 has increased to 1.72 from 1.22 compared to GO, due to the creation of new and smaller graphitic domains.[33] For the spectrum of GO, the intensity of D band is higher than that of G band, which can be attributed to partial reduction of GO during the freeze-drying process. The result of Raman spectra implies the effective reduction of GO to rGO during the reaction, which has also verified the result of FTIR spectra.

As displayed in Fig. 3, XRD analysis was applied to investigate the crystalline structures and structural changes of CZS, GO, and CZS/rGO-4. It is obvious that the XRD pattern of CZS (curve a in Fig. 3) exhibits several diffraction peaks at $2\theta$ = 27.216°, 27.731°, 29.364°, 32.863°, 48.017°, 52.712° and 59.339°, corresponding to (100), (101), (102), (103), (006), (110), (108), and (116) planes of the hexagonal phase of CuS (JCPDS no. 06-0464) respectively. Besides, the diffraction peaks at $2\theta$ = 28.650°, 48.017°, 56.518° are corresponded to the (111), (220), and (311) planes of the cubic phase of ZnS (JCPDS no. 05-0566). The sharp and narrow peaks manifest the high crystalline structure of the sample. The sharp peak at $2\theta$ = 9.96° assigned to the (001) reflection of GO is observed in Fig. 3(b), implying the well-ordered lamellar structure of GO.[34] The XRD pattern of CZS/rGO-4 shows similar diffraction peaks with that of CZS, indicating that CZS is a significant component of CZS/rGO-4, and the addition of rGO does not impede the crystal growth of CZS. The characteristic peak of GO at $2\theta$ = 9.96° does not exist in Fig. 3(c), which can be attributed to the effective reduction of GO to rGO in CZS/rGO-4. In addition, the absence of the typical stacking peak of graphite at about 26° indicates not only that the CZS particles homogeneously distribute on the rGO sheets, it would also illustrate that the rGO sheets do not stack and conglomerate after reduction. Finally, there are no relevant characteristic peaks for other impurities observed in

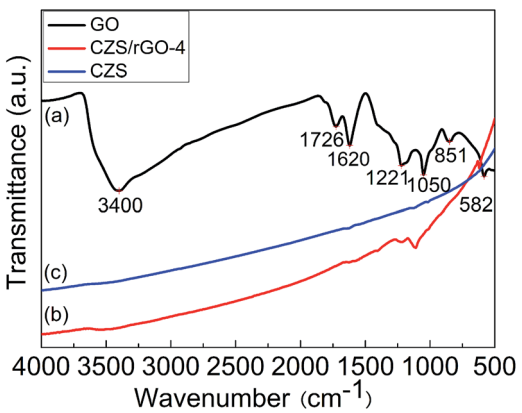


Fig. 1 FTIR spectra of (a) GO; (b) CZS/rGO-4; (c) CZS.

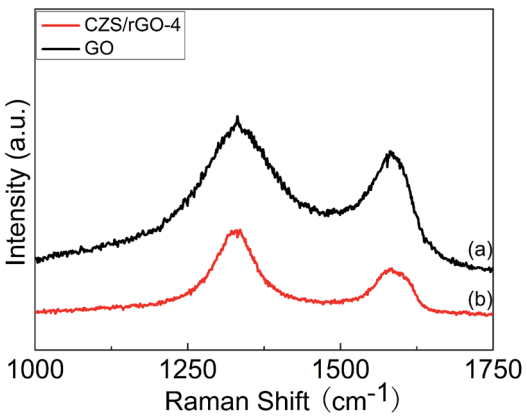


Fig. 2 Raman spectra of (a) GO; (b) CZS/rGO-4.

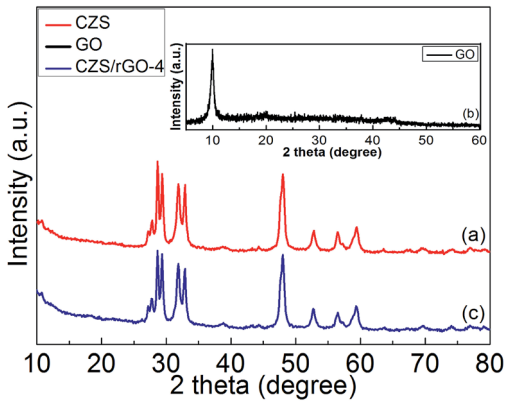


Fig. 3 XRD patterns of (a) CZS; (b) GO; (c) CZS/rGO-4.

the XRD pattern of CZS/rGO-4, indicating the well synthesis of the sample.[35,36]

The direct information of structure and morphology of the as-synthesized products can be easily received through the SEM images. As can be seen in Fig. 4(a), the liquid graphite oxide (GO) without performing any exfoliation treatment is of lamellar structure and possesses relatively large superficial area. In contrast, Fig. 4(b) presents that the rGO sheets originating from the reduction of graphite oxide are of stacked structure. It is obvious to deduce that GO sheets are of more excellent dispersibility and larger superficial area in aqueous solution than rGO sheets. CZS particles, with hierarchical structure, are displayed in Fig. 4(c). They are flower-like microspheres, constructed by nanoplates, and their average diameter is about 3 μm. It can be seen from Fig. 4(d) that CZS particles are decorated between rGO sheets homogeneously with intimate interfacial contact. Neither the CZS particles nor the rGO sheets seriously conglomerate during the reaction, because the loading of CZS particles inhibits the rGO sheets from stacking together, and the large surface area of rGO sheets serves as a two-dimensional supporting matrix for CZS particles to spread out uniformly. The analysis of SEM images is in accordance with the results of XRD analysis, which has further affirmed the successful synthesis of CZS/rGO-4.

The TGA curves of GO, CZS and CZS/rGO-4 are shown in Fig. 5. The TGA pattern of GO (curve a in Fig. 5) exhibits a two-step weight loss. The first weight loss takes place before 300 °C, due to the loss of the oxygen-containing groups in GO structure. The second one starts approximately at 450 °C, which can be attributed to most of the oxygen-containing functional groups being removed from the GO and completely decomposed after about 540 °C.[37] According to the TGA curves of CZS (curve b in Fig. 5) and CZS/rGO-4 (curve c in Fig. 5), the weight loss and weight gain of CZS/rGO-4 occur at a lower temperature than that of CZS, and the weight loss of CZS/rGO-4 is more, because of the oxidation of carbon.[38] The weight loss (150–330 °C) is also partially attributed to the transformation from CuS to $Cu_{1.8}S$ and $Cu_2S$. In the next step, the weight increase corresponds to the formation of $CuO{\cdot}CuSO_4$ and $CuSO_4$. CZS/rGO-4 contains less content of CZS because of the introduction of rGO, which induces the less weight gain of CZS/rGO-4 than that of CZS.[39]

The optical properties of the as-prepared samples were characterized by the UV-vis adsorption spectra with the scanning range from 200 nm to 800 nm (shown in Fig. S1†). It is obvious that all the spectra have a broad adsorption region of 580–700 nm and a relatively small adsorption region occurred below 400 nm. And the graphene-based samples have a broader adsorption region in the visible range. It demonstrates that the photocatalysts possess both UV and visible light response, which allows them to be excellent candidates in photocatalystic field making full use of solar energy.[40]

The photocatalytic activity of as-synthesized composites was evaluated by photocatalytic degradation of MB solution under light irradiation with the presence of $H_2O_2$. As shown in Fig. 6 A, in the first twenty minutes, it was mainly the adsorption process of photocatalysts without light irradiation and addition of $H_2O_2$, during which all the composites adsorbed as much MB molecules as they could to reach the adsorption–desorption equilibrium. Evidently, the larger amount of rGO one photocatalyst contained, the higher adsorption efficiency it possessed. The adsorption rates were 17.59%, 29.75%, 41.20%, 53.73%, and 80.92% respectively for the photocatalysts with different weight ratios of rGO ranging from 5% to 30%. However, the adsorption rate for CZS was only 7.21%, indicating

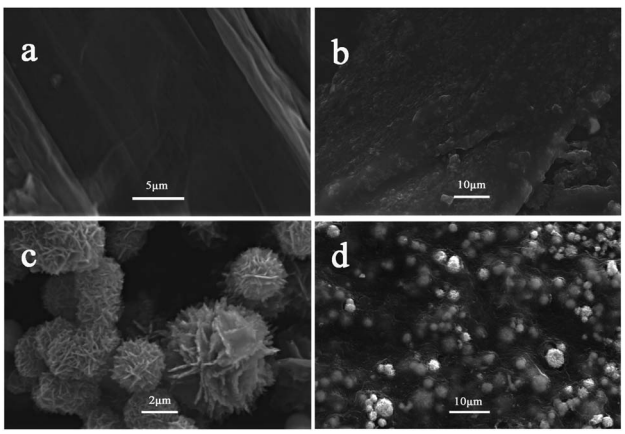


Fig. 4 SEM images of (a) GO; (b) rGO; (c) CZS; (d) CZS/rGO-4.

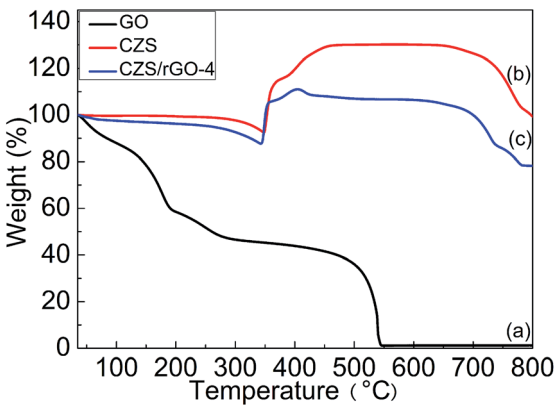


Fig. 5 TGA curves of (a) GO; (b) CZS; (c) CZS/rGO-4.

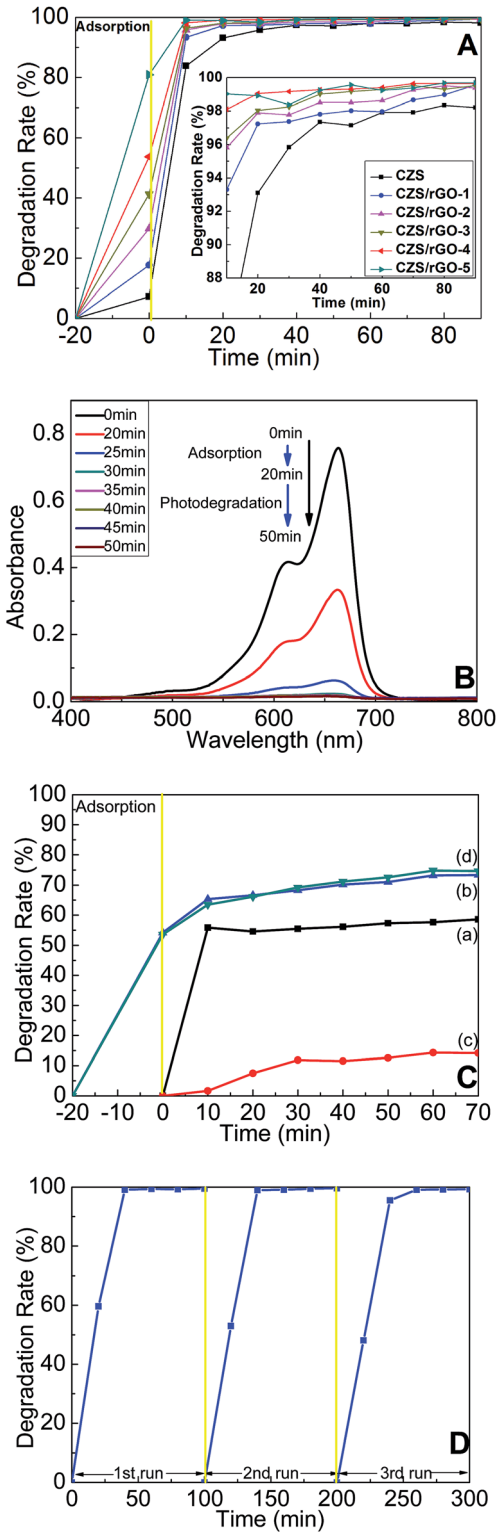


Fig. 6 (A) Degradation rate of MB in the presence of CZS and $H_2O_2$, CZS/rGO-1 and $H_2O_2$, CZS/rGO-2 and $H_2O_2$, CZS/rGO-3 and $H_2O_2$, CZS/rGO-4 and $H_2O_2$, and CZS/rGO-5 and $H_2O_2$ respectively; (B) UV-vis adsorption spectra of MB aqueous solutions with CZS/rGO-4 and $H_2O_2$ presence at different time intervals; (C) removal rate of MB in the presence of (a) CZS/rGO-4 without light irradiation; (b) CZS/rGO-4 with light irradiation; (c) $H_2O_2$ with light irradiation; (d) CZS/rGO-4 and $H_2O_2$ without light irradiation; (D) repetitive use of CZS/rGO-4.

that the introduction of rGO could dramatically increase the adsorption capacity of the photocatalysts and further facilitate the removal efficiency of pollutants. After being exposed to light irradiation for 20 min, most of the MB was eliminated in the presence of $H_2O_2$ and graphene-based photocatalysts. For example, the removal rates of MB were 99.05% and 98.92% for CZS/rGO-4 and CZS/rGO-5, which were higher than 93.10% for pure CZS. Compared to CZS/rGO-4, CZS/rGO-5 exhibited less stable photocatalytic efficiency, and had higher preparation cost because of the higher content of rGO. Furthermore, it would take 80 min, 70 min and 40 min respectively for CZS/rGO-1, CZS/rGO-2 and CZS/rGO-3 to eliminate more than 99% of MB in the presence of $H_2O_2$. While for CZS composite, the MB removal efficiency could hardly reach 99% in 90 min. According to the experimental results, all the graphene-based composites showed more outstanding photocatalytic performance than CZS. In addition, utilizing CZS/rGO-4 to remove MB could greatly shorten the reaction time compared with the other prepared photocatalysts. Thus it would be quite reasonable to infer that CZS/rGO-4 is the most suitable photocatalyst for practical application of all. Fig. 6B shows the temporal evolution of UV-vis adsorption spectra of MB solution during the photocatalytic reaction with $H_2O_2$ and CZS/rGO-4 presence. As can be seen, the characteristic peak of MB at 663 nm decreased gradually. In the first twenty minutes, the great decrease of the peak was ascribed to the adsorption of CZS/rGO-4 for MB. After exposure to light irradiation for 15 min, the adsorption peak almost disappeared, and no new peaks were observed, which demonstrated that MB was successfully eliminated by CZS/rGO-4. The results of blank experiments were displayed in Fig. 6C. According to the adsorption experiment of CZS/rGO-4 (curve a in Fig. 6C) performing in the dark, CZS/rGO-4 reached the adsorption–desorption equilibrium within 20 min. The result of photocatalytic reaction with only CZS/rGO-4 presence under light irradiation (curve b in Fig. 6C) showed higher MB removal rate than that in Fig. 6C(a), indicating that the degradation of MB was mainly attributed to the photocatalytic activity of CZS/rGO-4. As shown in Fig. 6C(c) and(d), $H_2O_2$ could only degrade about 14% of MB under light irradiation in 70 min, and about 75% of MB was eliminated with the presence of CZS/rGO-4 and $H_2O_2$ under the dark condition, mainly owning to the adsorption capacity of rGO and the oxidative capacity of $H_2O_2$. The stability test of CZS/rGO-4 applied to photodegrade MB under illumination was carried out and illustrated in Fig. 6D. The adsorption efficiency of CZS/rGO-4 only decreased a little after reuse every time, indicating that the MB molecules adsorbed on the surface of photocatalyst were finally decomposed. In addition, there was no significant decrease in photodegradation efficiency after reuse for three cycles, suggesting that CZS/rGO-4 is a promising photocatalyst for recyclable utilization.

The reduced graphene oxide loaded CuS/ZnS has rarely been reported. Compared to another rGO-ZnS/CuS composite reported by Zeng,[36] the as-prepared CZS/rGO-4 composite exhibits better crystalline structure, morphology and photocatalytic performance.

The possible mechanism of photocatalytic degradation of MB using CZS/rGO-4 as the photocatalyst is depicted as shown in Scheme 2. According to the IFCT (interfacial charge transfer) mechanism,[41] electrons in VB of ZnS can be excited by light irradiation and transfer to CuS clusters, leading to the partial reduction of CuS to $Cu_2S$. Because of the intimate contact of CZS particles and rGO sheets, as well as the excellent conductivity of rGO, the excited electrons in the CB of CuS/$Cu_2S$ clusters are most likely to transfer to rGO that acts as the electron collector and transporter. $O_2$ is able to scavenge photoinduced electrons to form $O_2^-$, and then reacts with $H_2O$ to generate hydroxyl radicals. During the whole photocatalytic process, $H_2O_2$ can finally become hydroxyl radicals, which play an extremely important role in MB degradation. The dyes adsorbed on the surface of photocatalyst can be rapidly decomposed to $CO_2$, $H_2O$ and small organic compounds by hydroxyl radicals. In addition, the holes in the VB of ZnS, on one hand, can destroy MB molecules directly; on the other hand, they prefer to react with adsorbed water or hydroxyl ions to generate hydroxyl radicals. All the phenomena aforementioned are favorable to suppressing the recombination of electron–hole pairs, and consequently improve the photocatalytic activity of CZS/rGO-4. At last, the removal of MB molecules adsorbed on the surface of photocatalyst breaks the adsorption–desorption equilibrium, and more MB molecules in the solution would adsorb on the surface of photocatalyst to construct a new equilibrium and finally be decomposed.[42,43]

The most critical factors associated with rGO that cause the great enhancement of MB degradation efficiency are concluded as follows. Firstly, due to the large specific surface area, rGO sheets can not only act as an ideal matrix for the distribution of CZS particles, they would also provide a larger place for the photodegradation reaction to take place. Additionally, the effective adsorption of MB molecules on the surface of rGO can enormously shorten the reaction distance of hydroxyl radicals and MB molecules, which consequently results in the improvement of photocatalytic efficiency. The adsorption can be ascribed to strong electrostatic force and π–π stacking interaction between rGO and MB molecules. Last but not least, the extraordinary conductivity of rGO significantly facilitates the mobility of photogenerated electrons and inhibits the recombination of charge carriers.[44–46]

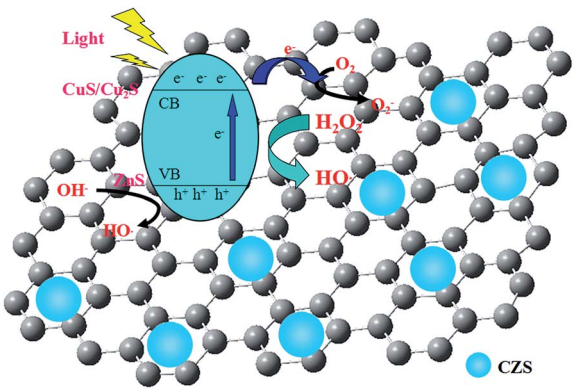


Scheme 2 The mechanism of photocatalytic degradation of MB by CZS/rGO.

## Conclusions

In summary, a series of CZS/rGO composites with different weight ratios of rGO were successfully synthesized *via* a sonochemical process, using CZS and GO as the initial reagents. CZS microspheres were homogeneously decorated on the surface of rGO sheets, which effectively hindered the aggregation of rGO sheets. In addition, all the graphene-based composites were of improved photocatalytic efficiency in the process of photocatalytic degradation of MB in comparison to the bare CZS microspheres. CZS/rGO-4 was able to eliminate more than 99% of MB within 20 min, utilizing both UV and visible light, and exhibited no significant decrease in photodegradation efficiency after reuse in three cycles. The introduction of reduced graphene oxide to the hybrid photocatalysts has a critical effect on the photocatalytic activity enhancement, it would not only facilitate the transportation of excited electrons and suppress the recombination of charge carriers, the giant two-dimensional rGO sheets would also be capable of increasing the adsorption capacity for organic molecules significantly. The results demonstrate that CZS/rGO composites used as novel photocatalysts have enormous potential for photodegradation of organic pollutants.

## Acknowledgements

This project was financially supported by the National Natural Science Foundation of China (nos 51472012) and supported by the Fundamental Research Funds for the Central Universities.

## Notes and references

1 L. J. Zhang, T. F. Xie, D. J. Wang, S. Li, L. L. Wang, L. P. Chen and Y. C. Lu, *Int. J. Hydrogen Energy*, 2013, **38**, 11811–11817.
2 H. S. Kim, D. Kim, B. S. Kwak, G. B. Han, M. H. Um and M. Kang, *Chem. Eng. J.*, 2014, **243**, 272–279.
3 L. Chen, X. Li, Y. Wang, C. Gao, H. Zhang, B. Zhao, F. Teng, J. Zhou, Z. Zhang, X. Pan and E. Xie, *J. Power Sources*, 2014, **272**, 886–894.
4 J. Zhang, Y. Hu, X. Jiang, S. Chen, S. Meng and X. Fu, *J. Hazard. Mater.*, 2014, **280**, 713–722.
5 Z. Yao, L. Wang, Y. Zhang, Z. Yu and Z. Jiang, *Int. J. Hydrogen Energy*, 2014, **39**, 15380–15386.
6 J. S. Chen, F. Xin, S. Y. Qin and X. H. Yin, *Chem. Eng. J.*, 2013, **230**, 506–512.
7 H. X. Sang, X. T. Wang, C. C. Fan and F. Wang, *Int. J. Hydrogen Energy*, 2012, **37**, 1348–1355.
8 J. S. Hu, L. L. Ren, Y. G. Guo, H. P. Liang, A. M. Cao, L. J. Wan and C. L. Bai, *Angew. Chem.*, 2005, **117**, 1295–1299.
9 Y. C. Weng, Y. D. Chou, C. J. Chang, C. C. Chan, K. Y. Chen and Y. F. Su, *Electrochim. Acta*, 2014, **125**, 354–361.
10 Q. Wang, G. Yun, Y. Bai, N. An, Y. Chen, R. Wang, Z. Lei and W. S. Guan, *Int. J. Hydrogen Energy*, 2014, **39**, 13421–13428.

11 Q. Wang, N. An, Y. Bai, H. Hang, J. Li, X. Lu, Y. Liu, F. Wang, Z. Li and Z. Lei, *Int. J. Hydrogen Energy*, 2013, **38**, 10739–10745.
12 U. T. D. Thuy, N. Q. Liem, C. M. A. Parlett, G. M. Lalev and K. Wilson, *Catal. Commun.*, 2014, **44**, 62–67.
13 X. Z. Zhou, X. Huang, X. Y. Qi, S. X. Wu, C. Xue, F. Y. C. Boey, Q. Y. Yan, P. Chen and H. Zhang, *J. Phys. Chem. Lett.*, 2009, **113**, 10842–10846.
14 S. Akcoltekin, M. E. I. Kharrazi, B. Kohler, A. Lorke and M. Schleberger, *Nanotechnology*, 2009, **20**, 155601.
15 A. Reina, X. T. Jia, J. Ho, D. Nezich, H. B. Son, V. Bulovic, M. S. Dresselhaus and J. Kong, *Nano Lett.*, 2009, **9**, 30–35.
16 V. Borovikov and A. Zangwill, *Phys. Rev. B: Condens. Matter Mater. Phys.*, 2009, **80**, 121406.
17 N. Liu, F. Luo, H. Wu, Y. Liu, C. Zhang and J. Chen, *Adv. Funct. Mater.*, 2008, **18**, 1518–1525.
18 H. J. Shin, K. K. Kim, A. Benayad, S. M. Yoon, H. K. Park, I. S. Jung, M. H. Jin, H. K. Jeong, J. M. Kim, J. Y. Choi and Y. H. Lee, *Adv. Funct. Mater.*, 2009, **19**, 1987–1992.
19 M. Zhou, Y. Wang, Y. Zhai, J. Zhai, W. Ren, F. Wang and S. Dong, *Chem.–Eur. J.*, 2009, **15**, 6116–6120.
20 L. Liu, J. Liu and D. D. Sun, *Catal. Sci. Technol.*, 2012, **2**, 2525–2532.
21 X. X. Wei, C. M. Chen, S. Q. Guo, F. Guo, X. M. Li, X. X. Wang, H. T. Cui, L. F. Zhao and W. Li, *J. Mater. Chem. A*, 2014, **2**, 4667–4675.
22 X. Zhao, F. Zhang, D. Lu, Y. Du, W. Ye and C. Wang, *Anal. Methods*, 2013, **5**, 3992–3998.
23 J. Bai and X. Jiang, *Anal. Chem.*, 2013, **85**, 8095–8101.
24 H. Zhang, X. J. Lv, Y. M. Li, Y. Wang and J. H. Li, *ACS Nano*, 2009, **4**, 380–386.
25 J. S. Lee, K. H. You and C. B. Park, *Adv. Mater.*, 2012, **24**, 1084–1088.
26 Q. Xiang, J. Yu and M. Jaroniec, *Chem. Soc. Rev.*, 2012, **41**, 782–796.
27 X. An and J. C. Yu, *RSC Adv.*, 2011, **1**, 1426–1434.
28 X. H. Guan, P. Qu, X. Guan and G. S. Wang, *RSC Adv.*, 2014, **4**, 15579–15585.
29 D. Chen, L. Li and L. Guo, *Nanotechnology*, 2011, **22**, 325601.
30 W. F. Chen, L. F. Yan and P. R. Bangal, *J. Phys. Chem. C*, 2010, **114**, 19885–19890.
31 C. Park, T. Ghosh, Z. Meng, U. Kefayat, N. Vikram and W. Oh, *Chin. J. Catal.*, 2013, **34**, 711–717.
32 Y. Sun, Q. Wu and G. Shi, *Energy Environ. Sci.*, 2011, **4**, 1113–1132.
33 C. Chen, W. M. Cai, M. C. Long, B. X. Zhou, Y. H. Wu, B. Y. Wu and Y. J. Feng, *ACS Nano*, 2010, **4**, 6425–6432.
34 H. Sun, L. Cao and L. Lu, *Nano Res.*, 2011, **4**, 550–562.
35 L. Jia, D. H. Wang, Y. X. Huang, A. W. Xu and H. Q. Yu, *J. Phys. Chem. C*, 2011, **115**, 11466–11473.
36 B. Zeng, X. Chen, C. Chen, X. Ning and W. Deng, *J. Alloys Compd.*, 2014, **582**, 774–779.
37 Z. Y. Lin, Y. G. Yao, Z. Li, Y. Liu, Z. Li and C. P. Wong, *J. Phys. Chem. C*, 2010, **114**, 14819–14825.
38 X. J. Zhang, G. S. Wang, Y. Z. Wei, L. Guo and M. S. Cao, *J. Mater. Chem. A*, 2013, **1**, 12115–12122.
39 H. T. Zhu, J. X. Wang and D. X. Wu, *Inorg. Chem.*, 2009, **48**, 7099–7104.
40 Y. Zhang, J. Tian, H. Li, L. Wang, X. Qin, A. M. Asiri, A. O. Al-Youbi and X. Sun, *Langmuir*, 2012, **28**, 12893–12900.
41 J. G. Yu, J. Zhang and S. W. Liu, *J. Phys. Chem. C*, 2010, **114**, 13642–13649.
42 X. Liu, L. Pan, T. Lv, G. Zhu, Z. Sun and C. Sun, *Chem. Commun.*, 2011, **47**, 11984–11986.
43 J. Qian, K. Wang, Q. Guan, H. Li, H. Xu, Q. Liu, W. Liu and B. Qiu, *Appl. Surf. Sci.*, 2014, **288**, 633–640.
44 Y. Wang, L. Zhang, H. Jiu, N. Li and Y. Sun, *Appl. Surf. Sci.*, 2014, **303**, 54–60.
45 H. N. Tien, V. H. Luan, L. T. Hoa, N. T. Khoa, S. H. Hahn, J. S. Chung, E. W. Shin and S. H. Hur, *Chem. Eng. J.*, 2013, **229**, 126–133.
46 Z. Gao, N. Liu, D. Wu, W. Tao, F. Xu and K. Jiang, *Appl. Surf. Sci.*, 2012, **258**, 2473–2478.